Thermalization dynamics of bi-partite Bose-Hubbard models

Christine Khripkov[1], Doron Cohen[2], and Amichay Vardi[1]

[1]*Department of Chemistry, Ben-Gurion University of the Negev, Beer-Sheva 84105, Israel*
[2]*Department of Physics, Ben-Gurion University of the Negev, Beer-Sheva 84105, Israel*

We study the time evolution of a bi-partite Bose-Hubbard model prepared far from equilibrium. When the classical dynamics is chaotic, we observe ergodization of the number distribution and a constant increase of the entanglement entropy between the constituent subsystems until it saturates to thermal equilibrium values. No thermalization is obtained when the system is launched in quasi-integrable phase space regions.

I. INTRODUCTION

The study of thermalization in isolated systems with a finite number of degrees of freedom [1] goes back to the pioneering work of Fermi, Pasta, and Ulam (FPU) on 1D oscillator chains with interactions [2–4]. While FPU were not able to demonstrate thermalization and observed long time recurrences, it was later understood that the ergodization of the system depends on its degree of nonlinearity and is linked to the onset of hard dynamical chaos [5]. Thus, beyond a certain interaction strength threshold, at which the Kolmogorov-Arnold-Moser (KAM) phase-space surfaces [6] break down, thermalization-like behavior is observed. Dynamical chaos and KAM physics apply also to classical mechanical systems with very few degrees of freedom; this connection implies that contrary to the traditional perception of statistical physics as describing large systems with numerous degrees of freedom, equilibration and statistical behavior are relevant even for small chaotic systems [7–9].

Trying to extend this understanding to the quantum realm is not straightforward because strict dynamical chaos is absent in quantum mechanics, which is linear and quasi-periodic by construction. Consequently, many open issues pertaining to the long time dynamics of isolated quantum systems and their ergodization are still under active experimental and theoretical investigation [10–28]. These include the existence of universal criteria for equilibration and thermalization, the mechanism by which thermal equilibrium may be attained and the role of quantum signatures of chaos in it, the nature of the equilibrated quantum state, and unique quantum features such as many-body Anderson localization [29–31].

When a system is dynamically chaotic, classical trajectories uniformly cover the microcanonical energy shell. The semiclassical outcome of this ergodicity is that phase-space distributions associated with any quantum eigenstate with the same energy are smeared throughout this shell. As a result, expectation values calculated for arbitrary *individual* energy eigenstates coincide with microcanonical averages taken over the appropriate energy surface. This observation is known as the Eigenstate Thermalization Hypothesis (ETH) [13, 14] wherein thermalization occurs 'within individual eigenstates'. By contrast, when the system is classically integrable, different eigenstates sample different phase-space regions cor-responding to different periodic orbits within an energy shell and thus give different non-thermal expectation values.

Starting from a non-equilibrium initial state, the paradigm for attaining thermalization between coupled quantum subsystems is Linear Response Theory (LRT). If the underlying classical dynamics is chaotic, thermalization is attained via diffusive energy spreading in each of the constituent subsystems, in response to its coupling to the others, resulting in a linear growth of the subsystem energy variance. This diffusive process, described by a Fokker-Planck Equation (FPE) [22–28], eventually leads to the desired ergodization of the composite system over all accessible states within the initial microcanonical energy shell.

Linear response theory is quantitatively based on a Fermi-golden-rule (FGR) picture in which the rates of transitions between the energy eigenstates of either subsystem are given by first-order-perturbation-like matrix elements, but over long timescales that involve many perturbative orders. The diffusion coefficient D of the FPE is estimated from these rates by a Kubo formula [32, 33], which implies QCC in the evolution of the spreading subsystem energy distribution [34].

In previous works we have studied the equilibration of Bose-Hubbard models with three [24] or four [25] bosonic modes. The viability of LRT was tested and effective FPEs describing the evolution of the pertinent energy distributions were derived. The degree of thermalization was evaluated from the agreement between the long time subsystem energy distribution and an ergodic distribution proportional to the density of states. Here, we expand and complement these studies by a direct calculation of the von Neumann entanglement entropy between the constituent subsystems of a bi-partite N-boson system, demonstrating nearly complete thermalization when the corresponding classical motion is chaotic.

In Section II we review the model system, its quantum Hilbert space and the determination of classically chaotic regions. The dynamics of the inter-system particle number distribution and its long time stationary form are described in Section III, while the time evolution of the reduced subsystem entropies is presented in Section IV. Conclusions are provided in Section V.

II. MODEL SYSTEM

A. The four-mode Bose-Hubbard Hamiltonian

We employ the same model as in Ref. [25]: a system of N bosons in four second quantized modes. The dynamics is generated by the Bose-Hubbard Hamiltonian (BHH)

$$\mathcal{H} = \frac{U}{2} \sum_{j=0}^{3} \hat{n}_j^2 - \frac{\Omega}{2}(\hat{a}_1^\dagger \hat{a}_2 + \hat{a}_1^\dagger \hat{a}_3 + \text{h.c.}) + \mathcal{H}_P , \quad (1)$$

where the operators $\hat{a}_j$, $\hat{a}_j^\dagger$ and $\hat{n}_j = \hat{a}_j^\dagger \hat{a}_j$ annihilate, create and count particles in site j, U is the on-site interaction, and Ω couples a chain of three sites $j = 1, 2, 3$. The perturbation $\mathcal{H}_P$ generates transitions to an additional $j = 0$ site, namely,

$$\mathcal{H}_P = -\frac{\omega}{2} \sum_{j=1}^{3} (\hat{a}_0^\dagger \hat{a}_j + \text{h.c.}) . \quad (2)$$

Thus $\mathcal{H}$ describes a bi-partite system: a BHH *trimer* coupled to a *monomer* (see schematic illustration in Fig.1). Weak coupling between the two subsystems is assumed ($\omega \ll \Omega, NU$), and the interaction within the trimer is quantified by the dimensionless interaction parameter $u = NU/\Omega$. In the classical description each site is described by conjugate action angle variables (n_j, φ_j). The standard procedure [35] is to work with dimensionless variables. In particular, the scaled occupations are n_j/N, hence upon quantization the scaled Planck constant is $\hbar = 1/N$. The classical limit is attained by taking the limit $N \to \infty$ while keeping NU constant. In this limit quantum fluctuations diminish and the bosonic operators can be replaced by c-numbers. The semiclassical description becomes valid if $\hbar \ll 1$.

The above *trimer plus monomer* model is the minimal Bose-Hubbard configuration which allows chaos and thermalization, because the trimer subsystem is classically chaotic [36] while a dimer is not. Furthermore, this type of minimal configuration serves as the *building-block* for progressive thermalization of large arrays [37, 38].

B. Hilbert space of the unperturbed system

The trimer population $\hat{x} \equiv \hat{n}_1 + \hat{n}_2 + \hat{n}_3$ commutes with the unperturbed ($\omega = 0$) Hamiltonian $\mathcal{H}_0$, and therefore constitutes a good quantum number in the absence of coupling. The unperturbed spectrum is defined by the eigenstate equation

$$\mathcal{H}_0 |x, \nu_x\rangle = E_{x,\nu_x} |x, \nu_x\rangle , \quad (3)$$

where the tetramer states

$$|x, \nu_x\rangle = |x, \nu_x\rangle_T |N - x\rangle_M , \quad (4)$$

are products of trimer states $|x, \nu_x\rangle_T$ and monomer states $|N - x\rangle_M$. The index ν_x counts the possible trimer states
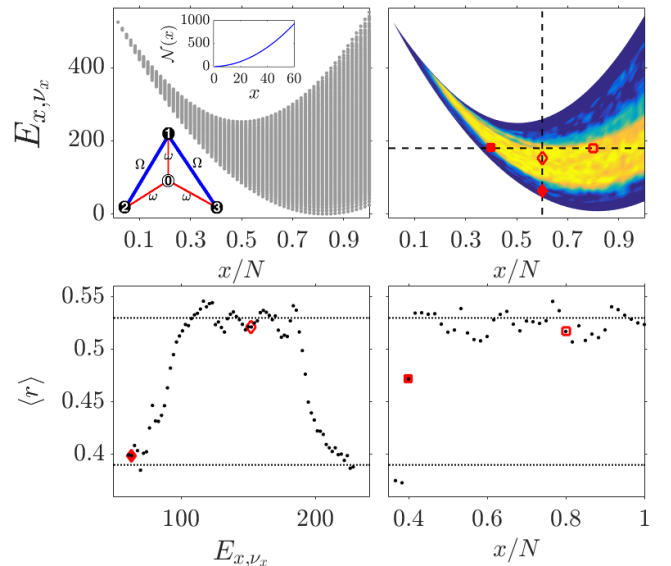

FIG. 1: Top left: The energy eigenstates of the unperturbed ($\omega = 0$) trimer-monomer model (lower inset), classified by the trimer population x. The parameters are $N = 60$, $NU = 20$, and $\Omega = 3.17$. The number of states in each x column $\mathcal{N}(x)$ is plotted in the upper inset. The spectrum is scaled by assigning a zero value to the lowest energy. Top right: Chaoticity map, showing the value of $\langle r \rangle$ throughout the allowed E, x range. Chaotic regions are yellow while integrable regions are blue. Lower panels: sections through the chaoticity map, along the lines marked in the top right panel. Horizontal dotted lines mark the expected values for Poissonian level spacing statistics (quasi-integrability) and for the level spacing statistics of the eigenstates of a Gaussian orthogonal ensemble of matrices (chaos). Symbols denote the four preparations used throughout the manuscript, two of which are chaotic (unfilled markers) and two lie in quasi-integrable or mixed regions (filled markers).

within a manifold that has x trimer particles. Thus, for any integer $x \in [0, N]$ we have $\nu_x \in [1, (x+1)(x+2)/2]$. Due to total particle number conservation, the monomer occupation is uniquely determined by x to be $N - x$.

In practice, since the model system is symmetric under exchange of trimer sites $j = 2$ and $j = 3$, the Hilbert space separates into two uncoupled subspaces spanned by the symmetric and antisymmetric superpositions of the four-site Fock states. Hence we can reduce the dimensionality of the many-body system with no change in its dynamics by selecting only the eigenstates belonging to a single symmetry subspace. Such separation is also a neccessary condition for the validity of the level-spacing analysis described in the next section. The resulting spectrum, classified into the different x manifolds, is plotted in Fig.1.
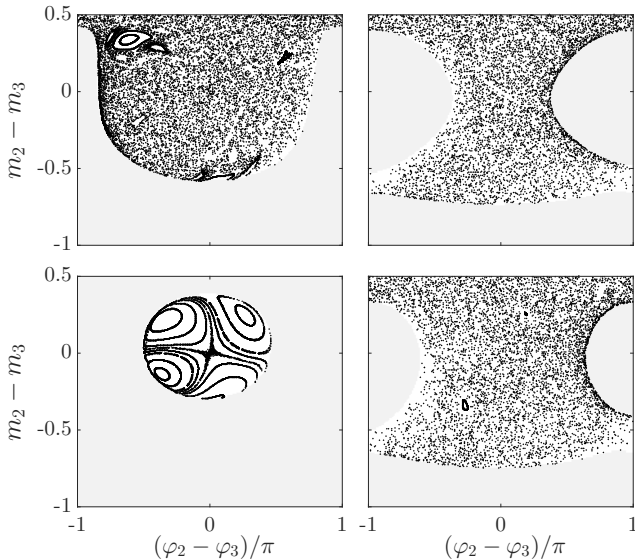
FIG. 2: Representative Poincare cross sections in the phase-space of the unperturbed system for the four initial conditions marked in Fig.1. Top panels refer to same-E points (squares), while bottom panels refer to same-x points (diamonds).

C. Classically chaotic region

The region where the trimer dynamics is classically chaotic is identified from the level-spacing statistics [39]. The adjacent spacings ratio

$$r_{\nu_x} = \min\{s_{\nu_x}, s_{\nu_x-1}\} / \max\{s_{\nu_x}, s_{\nu_x-1}\} \in [0,1] \quad (5)$$

where $s_{\nu_x} = E_{x,\nu_x+1} - E_{x,\nu_x}$ is averaged over a small energy window. When the motion is regular the energy levels are uncorrelated, resulting in Poissonian spacing statistics with $\langle r \rangle = \langle r \rangle_P = 2\ln 2 - 1 \approx 0.39$. By contrast, in regions of chaotic motion there is strong level repulsion, yielding Wigner-Dyson spacing statistics, with $\langle r \rangle = \langle r \rangle_{GOE} = 0.53$. Intermediate $\langle r \rangle$ values indicate a mixed phase space, containing both chaotic and quasi-integrable regions.

The obtained chaoticity map is plotted in Fig.1. It is in excellent agreement with previously obtained results of a Brody parameter map [25, 40]. Comparison with representative classical Poincare sections (see Fig.2) confirms that the classical motion is indeed chaotic in the high $\langle r \rangle$ regions and becomes quasi-integrable in low $\langle r \rangle$ regions .

III. COUPLING INDUCED DYNAMICS

A. Dynamics of subsystem number distribution

Coupling the trimer and monomer subsystems allows the transfer of particles and energy between them, thus inducing transitions along the occupation axis x. Given
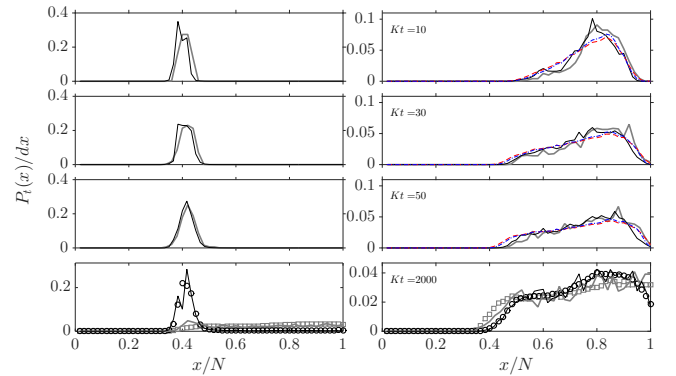

FIG. 3: Snapshots of the spreading x-distribution. The energy probability distribution $P_t(x)$ is plotted at the indicated times for the regular (left panels) and chaotic (right panels) same-E initial conditions marked by squares in Fig.1. The quantum (solid black) and the classical (wide solid gray) simulations are compared to the propagation of FGR (dashed red) and FPE (dash-dotted blue) equations. The symbols in lowest panels indicate the saturation profiles $P_{\text{erg}}(x)$ (squares) and $P_\infty(x)$ (circles).

the total system's time-dependent state

$$|\psi\rangle_t = \sum_{x,\nu_x} |x,\nu_x\rangle\langle x,\nu_x|\psi\rangle_t , \quad (6)$$

we focus our attention on the evolution of the trimer's number distribution

$$P_t(x) = \sum_{\nu_x} |\langle x,\nu_x|\psi\rangle|^2 , \quad (7)$$

starting with an initial state $|x_0,\nu_{x,0}\rangle$. This preparation is an eigenstate of the unperturbed Hamiltonian, but a far from equilibrium initial state for the combined system.

The weak coupling condition is obeyed by selecting $\omega = 0.1\Omega$. Representative examples for both classical and quantum mechanical evolution of the $P_t(x)$ distribution with four different initial states (marked in Fig.1) are shown in Fig.3 and Fig.4. Two of these preparations lie within the chaotic region whereas the other two reside in quasi-integrable regions. Similarly to the results of Refs. [23–25], the dynamics in the chaotic regime is characterized by stochastic-like diffusive spreading, eventually leading to a thermalized, ergodic x distribution. By contrast, launching the system in quasi-integrable regions, we obtain localized, non-ergodic distributions.

B. Quantitative description of $P_t(x)$ dynamics

As outlined in Ref. [25], the stochastic-like spreading dynamics of $P_t(x)$ in the chaotic regime, is captured by the master equation

$$\frac{\mathrm{d}}{\mathrm{d}t}p_{x',\nu'_{x'}} = -\sum_{x,\nu_x}\Gamma_{x,\nu_x,x',\nu'_{x'}}(p_{x',\nu'_{x'}} - p_{x,\nu_x}) , \quad (8)$$
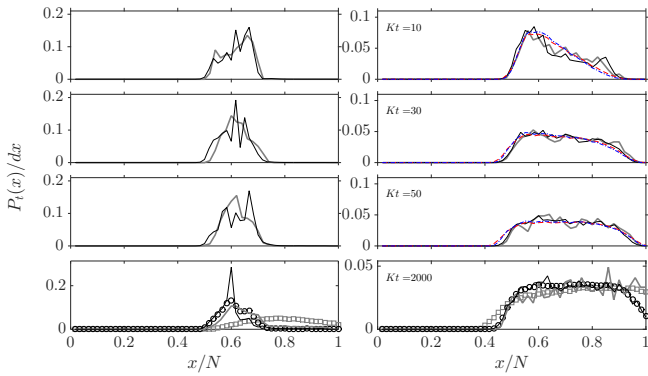
FIG. 4: Same as Fig. 3, only now for the same-x initial conditions marked by diamonds in Fig.1.

with rates given by a Fermi golden rule (FGR) prescription,

$$\Gamma_{x,\nu_x,x',\nu'_{x'}} = 2\pi\tau \ |\langle x',\nu'_{x'}|\mathcal{H}_p|x,\nu_x\rangle|^2 \ , \qquad (9)$$

and restricted to the band $|E_{x,\nu_x} - E_{x',\nu'_{x'}}| < 1/\tau$ where the bandwidth $1/\tau$ corresponds to the width of the power-spectrum of the perturbation, estimated by its variance

$$\frac{1}{\tau} \ = \ \sqrt{\langle x_0,\nu_{x,0}|\mathcal{H}^2|x_0,\nu_{x,0}\rangle - \langle x_0,\nu_{x,0}|\mathcal{H}|x_0,\nu_{x,0}\rangle^2} \ . \tag{10}$$

The kinetic equations (8) can be coarse grained to give a Fokker-Planck diffusion equation in x space [24, 25]

$$\frac{\partial}{\partial t}P(x) = \frac{\partial}{\partial x}\left[\tilde{g}(x)D(x)\frac{\partial}{\partial x}\left(\tilde{g}(x)^{-1}P(x)\right)\right] \ , \qquad (11)$$

where $\tilde{g}(x)$ is the density of states within the allowed energy shell. Proper evaluation of the diffusion coefficient $D(x)$ requires a resistor-network calculation (see Refs. [25, 41] for details).

The red dashed lines in Fig. 3 and Fig. 4 correspond to the propagation of Eq.(8) while blue dash-sotted lines correspond to the propagation of Eq.(11). The very good agreement with full quantum and semiclassical simulation validates these quantitative descriptions.

C. Equilibrium distributions

The FPE Eq.(11) describes a diffusive spreading process which continues until all accessible eigenstates are uniformly occupied, i.e. until the x-distribution saturates into the ergodic profile

$$P_{\mathrm{erg}}(x) = \frac{\tilde{g}(x)}{\sum_x \tilde{g}(x)} \ . \qquad (12)$$

On the other hand, the quantum eigenstate occupation may be expressed in the basis of exact eigenstates $|n\rangle$ of

the full Hamiltonian $\mathcal{H}$:

$$P_t(x,\nu_x) = \left|\langle x,\nu_x|e^{-i\mathcal{H}t}|x_0,\nu_{x,0}\rangle\right|^2$$

$$= \left|\sum_{n,m}\langle x,\nu_x|m\rangle\langle m|e^{-i\mathcal{H}t}|n\rangle\langle n|x_0,\nu_{x,0}\rangle\right|^2$$

$$= \left|\sum_n e^{-iE_n t}\langle x,\nu_x|n\rangle\langle n|x_0,\nu_{x,0}\rangle\right|^2 \ , \quad (13)$$

so that at sufficiently long times oscillating terms are averaged out and the x-distribution approaches the stationary form

$$P_\infty(x) = \sum_{\nu_x}\sum_n P(n|x,\nu_x)P(n|x_0,\nu_{x,0}) \ , \qquad (14)$$

where we have defined the local density of states (LDOS)

$$P(n|x,\nu_x) \equiv |\langle n|x,\nu_x\rangle|^2 \ . \qquad (15)$$

Thus, given an initial state $|x_0,\nu_{x,0}\rangle$, the long time probability of finding the system in any other eigenstate of the unperturbed system $|x,\nu_x\rangle$ is given by the vector product of their LDOS representations.

The final degree of ergodization can therefore be deduced from a simple comparison of $P_{\mathrm{erg}}(x)$ and $P_\infty(x)$ (markers in the bottom panels of Fig.3 and Fig.4). Initial preparations which reside in quasi-integrable phase space regions are superpositions of a fairly narrow band of exact eigenstates, thus giving localized, highly non-ergodic quantum saturation profiles. However, when the initial preparation is chaotic, it projects uniformly on all exact eigenstates, so that the quantum saturation profile becomes ergodic [42, 43].

Comparing the long time $P(x)$ distributions obtained in semiclassical and quantum simulations, it becomes clear that for quasi-integrable preparations both distributions remain localized. This quantum-classical correspondence clearly indicates that localization in the integrable domain is related to classical phase space structures. For chaotic preparations, as pointed above, both the classical and quantum distributions become nearly ergodic [44, 45]. However, while given a sufficient amount of time the classical distribution always approaches $P_{\mathrm{erg}}(x)$, the final quantum distribution $P_\infty(x)$ shows a residual localization, lacking weight at large and small x. This indicates purely quantum/many-body localization [46] which will be studied in detail in future work.

IV. DYNAMICS OF THE THE REDUCED SUBSYSTEM ENTROPY

Having established the ergodization of the population distribution between the two subsystems in the chaotic domain, we next demonstrate their thermalization by tracing the dynamics of the subsystems' entropy [47]. For
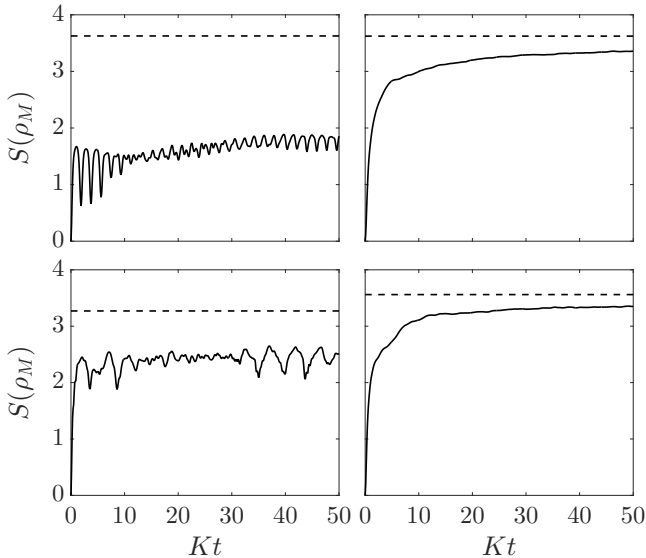
FIG. 5: The von Neumann entropy for the reduced density matrix of the monomer subsystem. Each panel represents one of the initial conditions marked in Fig. 1, keeping the same ordering as in Fig. 2. In the long time limit the entropy of the chaotic states (right panels) approach the ergodic value S_{erg} (dashed lines), while the entropy of the regular states (left panels) continues to oscillate about values significantly below S_{erg}.

this purpose we define the reduced trimer and monomer density operators

$$\rho_T = \text{Tr}_M (\rho)$$
$$= \sum_{x,\nu_x,\nu'_x} a_{x,\nu_x} a^*_{x,\nu'_x} |x,\nu_x\rangle_T \langle x,\nu'_x|_T \ , \qquad (16)$$

$$\rho_M = \text{Tr}_T (\rho)$$
$$= \sum_x \left(\sum_{\nu_x} a_{x,\nu_x} a^*_{x,\nu_x} \right) |x\rangle_M \langle x|_M \ , \qquad (17)$$

where

$$\rho = \sum_{x,\nu_x,x',\nu'_{x'}} a_{x,\nu_x} a^*_{x',\nu'_{x'}} |x,\nu_x\rangle \langle x',\nu'_{x'}| \qquad (18)$$

is the pure density matrix of the complete tetramer system and $a_{x,\nu_x} \equiv \langle x,\nu_x|\psi\rangle$. The trimer density matrix is thus block-diagonal and has the same rank as the full density matrix, while the monomer density matrix is a diagonal matrix of rank $N + 1$.

The entanglement between the constituent subsystems is quantified by the von Neumann entropy of their reduced density matrices

$$S_\alpha = \text{Tr} (\rho_\alpha \ln \rho_\alpha) \ , \qquad (19)$$

where $\alpha = T, M$. Starting with the factorizable state $|x_0, \nu_{x,0}\rangle$ ($S_T = S_M = 0$), the entropy of the two subsystems grows as they evolve and thermalize. Since the full system is isolated the subsystem entropies remain equal, i.e. $S_T = S_M = S$. Complete thermalization is indicated when S approaches the ergodic value

$$S_{\text{erg}} = \sum_x P_{\text{erg}}(x) \ln P_{\text{erg}}(x) \ . \qquad (20)$$

The time evolution of S is plotted in Fig. 5 for the four initial conditions considered in the previous sections. As expected, nearly complete thermalization is obtained for the chaotic cases, whereas if the system is launched in classically quasi-integrable regions, the entropy remains well below its equilibrium value.

V. CONCLUSIONS

Statistical thermodynamics relies on a number of postulates which are usually taken for granted. Given the system's configuration space Ω, the probability $P_t(s)$ of finding any configuration $s \in \Omega$ at time t, is assumed to obey a deterministic master equation. Equilibration is attained if $P_t(s)$ assumes a stationary form as $t \to \infty$. Thermalization requires that in addition, the probability currents between all pairs of configurations cancel out, resulting in detailed balance. An isolated system thermalizes into a uniform $P_t(s)$, i.e. regardless of initial conditions, each accessible configuration is visited with equal probability. This equal a priori probability postulate is the crux of equilibrium statistical physics.

In this work we have used a concrete quantum many-body system to address the origins of this fundamental framework of statistical physics and highlight the role of chaos in it. The schematic sketch of hopping between configurations is transformed explicitly into the FGR master equation Eq. (8). Equilibration of the classical and quantum distributions into the stationary limits of P_{erg} (Eq. (12)) and P_∞ (Eq. (14)) respectively, is clearly observed. And thermalization is evident from the asymptotic limit of the reduced subsystems' entropy. It is also evident that in the absence of chaos the system equilibrates over a restricted subset of accessible configurations but does not thermalize into the microcanonical equal probability distribution.

While the equilibrium quantum distribution P_∞ in the chaotic regime is nearly thermalized, its incomplete overlap with P_{erg} raises intriguing questions regarding the localization mechanism. The thermalization of the classical distribution at the same time suggests that this mechanism is an intricate many-body effect related to the quantum entanglement between particles. This issue will be addressed in a separate manuscript.

[1] J. R. Dorfman, *An Introduction to Chaos in Nonequilibrium Statistical Mechanics*, Cambridge University Press, Cambridge (1999).

[2] E. J. Fermi, J. Pasta, and S. Ulam, May 1955, Document LA-1940.

[3] D. K. Campbell, P. Rosenau, and G. M. Zaslavsky, Chaos **15**, 015101 (2005).

[4] M. A. Porter, N. J. Zabusky, B. Hu, and D. K. Campbell, Am. Sci. **97**, 214 (2009).

[5] F. M. Izrailev, and B. V. Chirikov, Sov. Phys. Dokl. **11**, 32 (1966).

[6] M. Tabor, *Chaos and integrability in nonlinear dynamics: An introduction*, Wiley, New York (1989).

[7] V. L. Berdichevsky, J. Appl.Math. Mech. **55**, 738 (1988).

[8] V. L. Berdichevsky, and M. V. Alberti, Phys. Rev. A **44**, 858 (1991).

[9] R. V. Jensen, and R.Shankar, Phys. Rev. Lett. **54**, 1879 (1985).

[10] T. Kinoshita, T. Wenger, and D. S. Weiss, Nature **440**, 900 (2006).

[11] S. Trotzky, Y-A. Chen, A. Flesch, I. P. McCulloch, U. Schollwöck, J. Eisert, and I. Bloch, Nat. Phys. **8**, 325 (2012).

[12] M. Gring, M. Kuhnert, T. Langen, T. Kitagawa, B. Rauer, M. Schreitl, I. Mazets, D. Adu Smith, E. Demler, and J. Schmiedmayer, Science **337**, 1318 (2012).

[13] J. M. Deutsch, Phys. Rev. A **43**, 2046 (1991).

[14] M. Srednicki, Phys. Rev. E **50**, 888 (1994).

[15] V. I. Yukalov, Laser Phys. Lett. **8**, 485 (2011).

[16] A. Polkovnikov, K. Sengupta, A. Silva, and M. Vengalattore, Rev. Mod. Phys. **83**, 863 (2011).

[17] M. Rigol, V. Dunjko, and M. Olshanii, Nature **452**, 854 (2008).

[18] A. C. Cassidy, D. Mason, V. Dunjko, and M. Olshanii, Phys. Rev. Lett. **102**, 025302 (2009).

[19] M. Eckstein, and M. Kollar, Phys. Rev. Lett. **100**, 120404 (2008).

[20] A. Pal, and D. A. Huse, Phys. Rev. B **82**, 174411 (2010).

[21] A. V. Ponomarev, S. Denisov, and P. Hänggi, Phys. Rev. Lett. **106**, 010405 (2011).

[22] G. Bunin, L. D'Alessio, Y. Kafri, and A. Polkovnikov, Nature Physics **7**, 913 (2011).

[23] C. Ates, J. P. Garrahan, and I. Lesanovsky, Phys. Rev. Lett. **108**, 110603 (2012).

[24] I. Tikhonenkov, A. Vardi, J. R. Anglin, and D. Cohen, Phys. Rev. Lett. **110**, 050401 (2013).

[25] C. Khripkov, A. Vardi, and D. Cohen, New. J. Phys. **17**, 023071 (2015).

[26] H. Niemeyer, D. Schmidtke, and J. Gemmer, Europhys. Lett. **101**, 10010 (2013).

[27] H. Niemeyer, K. Michielsen, H. De Raedt, and J. Gemmer, Phys. Rev. E **89**, 012131 (2014).

[28] C. Bartsch, R. Steinigeweg, and J. Gemmer, Phys. Rev. E **77**, 011119 (2008).

[29] L. Fleishman, and P. W. Anderson, Phys. Rev. B **21**, 2366 (1980).

[30] D. Basko, I. L. Aleiner, and B. Altshuler, Ann. Phys. **321**, 1126 (2006).

[31] Y. Bar Lev, and D. R. Reichman, eprint arXiv:1402.0502

[32] M. Wilkinson, J. Phys. A **21**, 4021 (1988).

[33] M. Wilkinson, and E. J. Austin, J. Phys. A **28**, 2277 (1995).

[34] D. Cohen, Phys. Rev. Lett. **82**, 4951 (1999).

[35] M. Chuchem, K. Smith-Mannschott, M. Hiller, T. Kottos, A. Vardi, and D. Cohen, Phys. Rev. A **82**, 053617 (2010).

[36] M. Hiller, T. Kottos, and T. Geisel, Phys. Rev. A **79**, 023621 (2009); and further references therein.

[37] D. M. Basko, Ann. Phys. **326**, 1577 (2011).

[38] H. Hennig, and R. Fleischmann, Phys. Rev. A **87**, 033605 (2013).

[39] V. Oganesyan, and D. A. Huse, Phys. Rev. B **75**, 155111 (2007).

[40] T. A. Brody, J. Flores, J. B. Fench, P. A. Mello, A. Pandey, and S. S. M. Wong, Rev. Mod. Phys. **53**, 385 (1981).

[41] D. Cohen, Physica Scripta **T151**, 014035 (2012).

[42] L. F. Santos, F. Borgonovi, and F. M. Izrailev, Phys. Rev. Lett. **108**, 094102 (2012).

[43] M. Rigol, and L. F. Santos, Phys. Rev. A **82**, 011604(R) (2010).

[44] A. J. Short, and T. C. Farrelly, New J. Phys. **14**, 013063 (2012).

[45] P. Reimann, and M. Kastner, New J. Phys. **14**, 043020 (2012).

[46] V. A. Yurovsky, and M. Olshanii, Phys. Rev. Lett. **106**, 025303 (2011).

[47] R. Kosloff, Entropy **15**, 2100 (2013).